

Laser-induced thermophoresis of individual particles in a viscous liquid

Ross T. Schermer,^{1,*} Colin C. Olson,^{1,2} J. Patrick Coleman,^{1,2} and Frank Bucholtz¹

¹Optical Sciences Division, U.S. Naval Research Laboratory, 4555 Overlook Avenue, SW, Washington, DC, USA
²Permanent Address: Global Defense Technology & Systems, Inc., 2200 Defense Highway, Suite 405, Crofton, MD, USA

*ross.schermer@nrl.navy.mil

Abstract: This paper presents a detailed investigation of the motion of individual micro-particles in a moderately-viscous liquid in direct response to a local, laser-induced temperature gradient. By measuring particle trajectories in 3D, and comparing them to a simulated temperature profile, it is confirmed that the thermally-induced particle motion is the direct result of thermophoresis. The elevated viscosity of the liquid provides for substantial differences in the behavior predicted by various models of thermophoresis, which in turn allows measured data to be most appropriately matched to a model proposed by Brenner. This model is then used to predict the effective force resulting from thermophoresis in an optical trap. Based on these results, we predict when thermophoresis will strongly inhibit the ability of radiation pressure to trap nano-scale particles. The model also predicts that the thermophoretic force scales linearly with the viscosity of the liquid, such that choice of liquid plays a key role in the relative strength of the thermophoretic and radiation forces.

OCIS codes: (350.5340) Photothermal effects; (140.7010) Laser trapping; (170.4520) Optical confinement and manipulation; (160.4236) Nanomaterials.

References and links

1. R. Piazza and A. Parola, "Thermophoresis in colloidal suspensions," *J. Phys. Condens. Matter* **20**(15), 153102 (2008).
2. J. K. Platten, "The Soret effect: a review of recent experimental results," *J. Appl. Mech.* **73**(1), 5–15 (2006).
3. H. Brenner, "Navier-Stokes revisited," *Physica A* **349**(1-2), 60–132 (2005).
4. G. S. McNab and A. Meisen, "Thermophoresis in liquids," *J. Colloid Interface Sci.* **44**(2), 339–346 (1973).
5. H. Brenner and J. R. Bielenberg, "A continuum approach to phoretic motions: thermophoresis," *Physica A* **355**(2-4), 251–273 (2005).
6. M. E. Schimpf and S. N. Semenov, "Mechanism of polymer thermophoresis in nonaqueous solvents," *J. Phys. Chem. B* **104**(42), 9935–9942 (2000).
7. S. Semenov and M. Schimpf, "Thermophoresis of dissolved molecules and polymers: Consideration of the temperature-induced macroscopic pressure gradient," *Phys. Rev. E Stat. Nonlin. Soft Matter Phys.* **69**(1), 011201 (2004).
8. E. Ruckenstein, "Can phoretic motions be treated as interfacial tension gradient driven phenomena," *J. Colloid Interface Sci.* **83**(1), 77–81 (1981).
9. A. Parola and R. Piazza, "Particle thermophoresis in liquids," *Eur Phys J E Soft Matter* **15**(3), 255–263 (2004).
10. S. Dühr and D. Braun, "Why molecules move along a temperature gradient," *Proc. Natl. Acad. Sci. U.S.A.* **103**(52), 19678–19682 (2006).
11. H. Brenner, "A nonmolecular derivation of Maxwell's thermal creep boundary condition in gases and liquids via application of the LeChatelier-Braun principle to Maxwell's thermal stress," *Phys. Fluids* **21**(5), 053602 (2009).
12. O. Jovanovic, "Photophoresis: light-induced motion of particles suspended in gas," *J. Quant. Spectrosc. Radiat. Transf.* **110**(11), 889–901 (2009).
13. A. Ashkin, *Optical Trapping and Manipulation of Neutral Particles Using Lasers* (World Scientific, 2006).
14. A. Regazzetti, M. Hoyos, and M. Martin, "Experimental evidence of thermophoresis of non-brownian particles in pure liquids and estimation of their thermophoretic mobility," *J. Phys. Chem. B* **108**(39), 15285–15292 (2004).
15. S. Dühr and D. Braun, "Thermophoretic depletion follows Boltzmann distribution," *Phys. Rev. Lett.* **96**(16), 168301 (2006).
16. R. Di Leonardo, F. Ianni, and G. Ruocco, "Colloidal attraction induced by a temperature gradient," *Langmuir* **25**(8), 4247–4250 (2009).
17. K. C. Neuman and S. M. Block, "Optical trapping," *Rev. Sci. Instrum.* **75**(9), 2787–2809 (2004).
18. J. R. Moffitt, Y. R. Chemla, S. B. Smith, and C. Bustamante, "Recent advances in optical tweezers," *Annu. Rev. Biochem.* **77**(1), 205–228 (2008).

Report Documentation Page

Form Approved
OMB No. 0704-0188

Public reporting burden for the collection of information is estimated to average 1 hour per response, including the time for reviewing instructions, searching existing data sources, gathering and maintaining the data needed, and completing and reviewing the collection of information. Send comments regarding this burden estimate or any other aspect of this collection of information, including suggestions for reducing this burden, to Washington Headquarters Services, Directorate for Information Operations and Reports, 1215 Jefferson Davis Highway, Suite 1204, Arlington VA 22202-4302. Respondents should be aware that notwithstanding any other provision of law, no person shall be subject to a penalty for failing to comply with a collection of information if it does not display a currently valid OMB control number.

1. REPORT DATE MAY 2011		2. REPORT TYPE		3. DATES COVERED 00-00-2011 to 00-00-2011	
4. TITLE AND SUBTITLE Laser-Induced Thermophoresis Of Individual Particles In A Viscous Liquid				5a. CONTRACT NUMBER	
				5b. GRANT NUMBER	
				5c. PROGRAM ELEMENT NUMBER	
6. AUTHOR(S)				5d. PROJECT NUMBER	
				5e. TASK NUMBER	
				5f. WORK UNIT NUMBER	
7. PERFORMING ORGANIZATION NAME(S) AND ADDRESS(ES) U.S. Naval Research Laboratory, 4555,Optical Sciences Division,4555 Overlook Avenue, SW,Washington,DC,20375				8. PERFORMING ORGANIZATION REPORT NUMBER	
9. SPONSORING/MONITORING AGENCY NAME(S) AND ADDRESS(ES)				10. SPONSOR/MONITOR'S ACRONYM(S)	
				11. SPONSOR/MONITOR'S REPORT NUMBER(S)	
12. DISTRIBUTION/AVAILABILITY STATEMENT Approved for public release; distribution unlimited					
13. SUPPLEMENTARY NOTES Optics Express, Vol 19, No 11, 23 May 2011					
14. ABSTRACT This paper presents a detailed investigation of the motion of individual micro-particles in a moderately-viscous liquid in direct response to a local, laser-induced temperature gradient. By measuring particle trajectories in 3D, and comparing them to a simulated temperature profile, it is confirmed that the thermally-induced particle motion is the direct result of thermophoresis. The elevated viscosity of the liquid provides for substantial differences in the behavior predicted by various models of thermophoresis, which in turn allows measured data to be most appropriately matched to a model proposed by Brenner. This model is then used to predict the effective force resulting from thermophoresis in an optical trap. Based on these results, we predict when thermophoresis will strongly inhibit the ability of radiation pressure to trap nano-scale particles. The model also predicts that the thermophoretic force scales linearly with the viscosity of the liquid, such that choice of liquid plays a key role in the relative strength of the thermophoretic and radiation forces					
15. SUBJECT TERMS					
16. SECURITY CLASSIFICATION OF:			17. LIMITATION OF ABSTRACT	18. NUMBER OF PAGES	19a. NAME OF RESPONSIBLE PERSON
a. REPORT	b. ABSTRACT	c. THIS PAGE			
unclassified	unclassified	unclassified	Same as Report (SAR)	17	

19. M. Dienerowitz, M. Mazilu, and K. Dholakia, "Optical manipulation of nanoparticles: a review," *J. Nanophotonics* **2**(1), 021875 (2008).
20. W. M. Haynes, ed., *CRC Handbook of Chemistry and Physics*, 91st ed., (CRC, 2010).
21. X. Ma, J. Q. Lu, R. S. Brock, K. M. Jacobs, P. Yang, and X.-H. Hu, "Determination of complex refractive index of polystyrene microspheres from 370 to 1610 nm," *Phys. Med. Biol.* **48**(24), 4165–4172 (2003).
22. T. P. Otanicar, P. E. Phelan, and J. S. Golden, "Optical properties of liquids for direct absorption solar thermal energy systems," *Sol. Energy* **83**(7), 969–977 (2009).
23. A. Yariv, *Optical Electronics in Modern Communications*, 5th ed. (Oxford, 1997).
24. T. A. Nieminen, V. L. Y. Loke, A. B. Stilgoe, G. Knöner, A. M. Brańczyk, N. R. Heckenberg, and H. Rubinsztein-Dunlop, "Optical tweezers computational toolbox," *J. Opt. A, Pure Appl. Opt.* **9**(8), S196–S203 (2007).
25. T. A. Nieminen, H. Rubinsztein-Dunlop, and N. R. Heckenberg, "Multipole expansion of strongly focused laser beams," *J. Quant. Spectrosc. Radiat. Transf.* **79–80**, 1005–1017 (2003).
26. T. A. Nieminen, H. Rubinsztein-Dunlop, and N. R. Heckenberg, "Calculation of the T-matrix: general considerations and application of the point-matching method," *J. Quant. Spectrosc. Radiat. Transf.* **79–80**, 1019–1029 (2003).
27. T. Sun and A. S. Teja, "Density, viscosity and thermal conductivity of aqueous solutions of propylene glycol, dipropylene glycol, and tripropylene glycol between 290 K and 460 K," *J. Chem. Eng. Data* **49**(5), 1311–1317 (2004).
28. E. Fällman and O. Axner, "Influence of a glass-water interface on the on-axis trapping of micrometer-sized spherical objects by optical tweezers," *Appl. Opt.* **42**(19), 3915–3926 (2003).
29. Y. Roichman, A. Waldron, E. Gardel, and D. G. Grier, "Optical traps with geometric aberrations," *Appl. Opt.* **45**(15), 3425–3429 (2006).
30. J. P. Holman, *Heat Transfer*, 9th ed. (McGraw Hill, 2002).
31. F. W. Schmidt, R. E. Henderson, and C. H. Wolgemuth, *Introduction to Thermal Sciences* (Wiley, 1984).
32. S. Dühr, S. Arduini, and D. Braun, "Thermophoresis of DNA determined by microfluidic fluorescence," *Eur Phys J E Soft Matter* **15**(3), 277–286 (2004).
33. T. Cosgrove, *Colloid Science: Principles, Methods and Applications* (Wiley, 2005).
34. J. Berg, *Wettability (Surfactant Science)* (CRC, 1993).
35. B. C. Hoke, Jr. and E. F. Patton, "Surface tensions of propylene glycol + water," *J. Chem. Eng. Data* **37**(3), 331–333 (1992).
36. K. K. Kundu and M. N. Das, "Autoprotolysis constants of ethylene glycol and propylene glycol and dissociation constants of some acids and bases in the solvents at 30° C," *J. Chem. Eng. Data* **9**(1), 82–86 (1964).
37. H. J. Butt, K. Graf, and M. Kappl, *Physics and Chemistry of Interfaces*, (Wiley, 2003).
38. H. Brenner, "Kinematics of volume transport," *Physica A* **349**(1-2), 11–59 (2005).
39. H. Bruus, *Theoretical Microfluidics* (Oxford, 2008).

1. Introduction

It has long been known that particles immersed in a gas or liquid will migrate in response to a thermal gradient, an effect known as thermophoresis. In liquids this leads to phenomena such as the Soret effect [1,2], in which mixtures tend to separate in response to a thermal gradient. In gases the origins of thermophoresis are reasonably well-understood, and the relationship between thermal gradient and induced motion can be related directly to the kinetic theory of gases [3]. For liquids, however, there are numerous contradictory theoretical descriptions [3–11], partially due to the lack of experimental data on single-particle motion [3,7], and partially to the fact that thermo-diffusion, having to do with the concentration of particles in a liquid, is most easily treated empirically [1].

In the context of laser trapping and manipulation of small particles, the thermal force induced by optical absorption *within a particle*, and the resulting temperature gradient (known as the indirect photophoretic force), has been well explored for particles suspended in a gas [12]. Indeed, this force forms the basis for the "radiometric barrier" which must be overcome to trap particles at low gas pressure [13]. In liquids, laser-induced thermo-diffusion of large collections of nanoparticles has also been studied, but primarily in the context of thermally-induced variations in steady-state particle concentration (i.e. the Soret effect) rather than the motion of individual particles. Empirical and theoretical models describing thermo-diffusion, however, tend to differ from the observed motion of individual particles in a liquid [3,14]. Studies of laser-induced thermophoresis of individual particles in liquids have also been performed [10,15,16], but quantitative results are generally limited to aqueous solutions, and thus provide limited data for the evaluation of theory. Such works also rely on very weakly-focused optical beams, quite different from that of typical optical tweezers.

For traditional (radiation-pressure-based) optical traps, the thermophoresis of individual particles in liquids has received little attention. This is due at least in part to the dominance of radiation pressure over thermal forces in typical optical trapping experiments, such that thermophoretic migration is not easily observed in a trap. A lack of theoretical understanding of thermophoresis in liquids, however, has also undoubtedly played a part. A consequence is that standard theoretical models for forces in an optical trap do not account for a thermophoretic force [17,18]. Given that thermophoresis is a proven method for manipulating groups of nano-scale particles in liquids, whereas radiation pressure struggles on the nano-scale [10,19], it is important to bridge the gap between the two phenomena.

This paper attempts to shed some light on the subject, by characterizing the laser-induced thermophoresis of individual microspheres in a moderately-viscous liquid (sixty times more viscous than water). The elevated viscosity of the liquid leads to substantial differences in the behavior predicted by various models of thermophoresis, thus allowing measured data to be most appropriately matched to a theoretical model proposed by Brenner. This model is then used to predict the effective force resulting from thermophoresis in an optical trap. Based on these results, we predict when thermophoresis will strongly inhibit the ability of radiation pressure to trap nano-scale particles. The model also predicts that the thermophoretic force scales linearly with the viscosity of the liquid, such that choice of liquid plays a key role in the relative strength of the thermophoretic and radiation forces.

2. Experiment

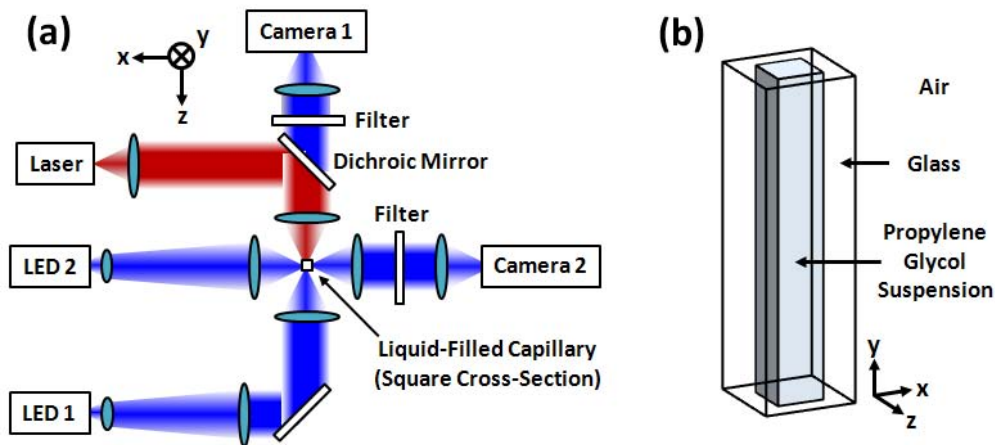


Fig. 1. Schematic diagrams of (a) the optical system used to manipulate and track particles in a liquid, and (b) the liquid-filled, square cross-section, glass capillary sample cell. The cell was held suspended in air by a rigid clamp, located 2.0 cm above the laser focus in the positive y -direction. Gravity was directed along the negative y -direction.

A schematic diagram of the experimental setup used to study laser thermophoresis in liquids is shown in Fig. 1. The system utilized a simple single-beam optical trap, formed by launching the output of an 808 nm distributed feedback laser diode through a collimating lens, reflecting it off of a dichroic mirror, and focusing to a spot with an infinity-corrected, 0.66 numerical aperture objective lens. At the focus of the trap was placed a sample cell, consisting of a liquid-suspension-filled, borosilicate glass capillary with square cross-section ($50\ \mu\text{m}$ inner width, $25\ \mu\text{m}$ wall thickness) and 5 cm length. The cell was oriented such that the capillary wall was normal to the incident beam, and its long axis was vertical (parallel to the force of gravity). It was held suspended in air by a rigid clamp, which first contacted the cell 2 cm above the beam focus. The cell extended roughly 1 cm below the beam focus. Due to the flat walls of the capillary, and the narrow thickness of fluid within, the position of individual particles in the liquid could be easily observed along two orthogonal directions. This allowed two CCD cameras, shown in Fig. 1, to image and track particle positions in 3D, one

measuring particle location (x,y) , and the other (y,z) . For the (y,z) view, a lower, 0.28 numerical aperture lens was used to provide greater depth of field. 3D video was acquired by triggering the exposure of both cameras simultaneously, at 30 frames per second with a common signal, and recording the images on a computer. Illumination of the cell was performed using a pair of white light emitting diodes (LEDs), which were chosen to prevent sample heating due to infrared absorption of the illumination source. The divergence of the trap beam was measured to be 36° in air, by profiling the beam intensity with a z-scanned mirror. The optical power of the trap beam was also measured to be 38 mW in air. After accounting for Fresnel reflections in the sample cell the power was estimated to be 35 mW in the liquid.

In order to investigate particle motion due to laser-induced thermophoresis, it was necessary to limit the relative strength of the radiation pressure produced on the particles in the sample cell. One option would have been to use a highly-absorptive liquid (or wavelength) to enhance the temperature gradient relative to the radiation pressure on the particle. An alternative was to reduce the radiation pressure on the particle, without significantly altering the optical absorption of the liquid. The latter was chosen for this experiment, because it was believed to provide a better representation of the thermal conditions in a typical optical trapping/manipulation experiment.

In order to reduce the radiation pressure on the particles, without resorting to extremely small particles which would be more susceptible to Brownian motion, it was necessary to reduce the refractive index contrast $\Delta n = n_p - n_l$ between the particle and liquid, where n_p and n_l are the refractive indices of the particle and liquid, respectively. This was accomplished by mixing dry silica microspheres ($n_p = 1.45$ [20]) with 99.5% pure propylene glycol (1,2 propanediol) ($n_l = 1.43$ [20]), forming a low-concentration, low index contrast ($\Delta n = 0.02$) suspension. The suspension was then placed in the sample cell via capillary action. In the small-particle limit, radiation pressure can be separated into gradient and scattering force components which scale roughly as Δn and $(\Delta n)^2$, respectively [17]. Thus, compared to polystyrene spheres in water ($\Delta n = 0.25$) [21], the radiation pressure in the experiment should have been substantially reduced. Furthermore, since the optical absorption of propylene glycol is similar to that of water [22], as is its thermal diffusivity, the temperature distribution within the cell should have been comparable to that of a water-filled cell. An additional advantage of propylene glycol was that it provided a relatively high viscosity, 0.055 kg/m·s, which served to dampen Brownian motion of the particles in the experiment, and to suppress convective flow.

Figure 2 presents a time-lapsed video ([Media 1](#)) of the laser-induced motion of two silica microspheres in propylene glycol. Time in the video has been scaled by a factor of 30, such that one second in the video corresponds to thirty seconds in the experiment. Also shown are curves representing the $1/e^2$ intensity limits of the optical beam, as calculated by approximating a Gaussian beam profile of the form

$$I(x, y, z) \cong \frac{2P}{\pi\omega^2(z)} \exp\left[\frac{-2(x^2 + y^2)}{\omega^2(z)}\right] \quad (1)$$

where

$$\omega(z) = \omega_0 \sqrt{1 + \left(\frac{z\lambda_0}{\pi n_l \omega_0^2}\right)^2}, \quad (2)$$

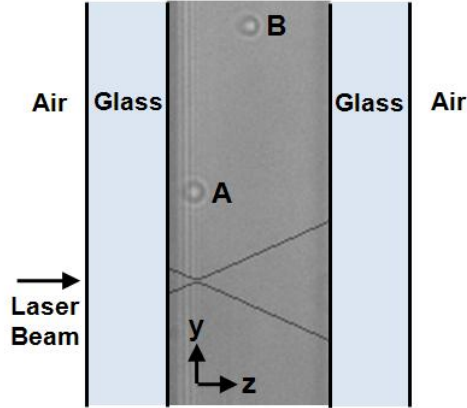


Fig. 2. Time-lapsed video (Media 1) of the motion of two silica microspheres, (A) and (B), suspended in propylene glycol, in response to a focused laser beam. Each second in the video corresponds to thirty seconds in the experiment. The $1/e^2$ intensity limits of the laser beam, calculated using Eqs. (1) and (2), have been overlaid in gray. The thicknesses of the cell walls and liquid region between were $25\ \mu\text{m}$ and $50\ \mu\text{m}$, respectively. Microsphere (A) falls into the beam, becomes trapped in (x,y) , and is subsequently pushed along the beam $24\ \mu\text{m}$ before being released from the 2D trap. Microsphere (B) falls past the beam without becoming trapped, but experiences a similar push when closest to the beam axis. Particle size is exaggerated due to imperfect focus.

$$\omega_0 = \frac{\lambda_0}{\pi n_l \tan \theta_{0l}} \approx \frac{\lambda_0}{\pi \tan \theta_{0a}}, \quad (3)$$

P is the optical power, λ_0 is the vacuum wavelength, ω_0 is size of the beam waist, and θ_{0l} and θ_{0a} are the beam divergences in liquid and air, respectively [23]. Using the measured beam divergence in air, the waist size was estimated to be $0.4\ \mu\text{m}$. The location of the beam waist in the video, which corresponded to the origin of the coordinate system, was calibrated by moving the cell in z with a precision micrometer to focus on different microspheres with camera 1, and noting their locations in the camera 2 view. Since the beam waist coincided with the image focus (in air), this calibration was taken as a reasonable estimate of the beam waist position. The location of the beam axis $(x,y) = (0,0)$ was readily determined by imaging the reflected beam profile with camera 1. With this calibration, the central axis of the capillary tube coincided with the coordinates $(x,z) = (-1.6,14)\ \mu\text{m}$.

Figure 2 demonstrates that the microspheres initially fell in the negative y direction, which was due to a combination of gravitational force (resisted by viscous drag) and a creeping laminar flow resulting from evaporation from the open ends of the capillary. Upon nearing the laser beam, microsphere A was pulled rapidly into the center of the beam, becoming trapped in x and y , and subsequently pushed along the beam a distance of $24\ \mu\text{m}$ before being released from the trap and resuming its downward motion. In the same timeframe, microsphere B passed by the optical beam, with no noticeable change in direction except when nearest the optical beam.

Figure 3 plots the positions of microspheres A and B in 3D as a function of time, which were determined by particle tracking analysis of the image sequences from both cameras. As shown, microsphere A was initially pulled into the beam and pushed rapidly towards the waist, and then upon passing the waist exhibited slow but relatively constant velocity along the direction of the beam. Past the beam waist, it moved with an average velocity $0.12\ \mu\text{m/s}$ over a $19\ \mu\text{m}$ distance, while at the same time remaining trapped in x and y . Microsphere B, on the other hand, which was offset from the beam axis by $-5.5\ \mu\text{m}$ in the x -direction, and therefore never trapped, exhibited a similar $0.11\ \mu\text{m/s}$ velocity when within $8\ \mu\text{m}$ of the beam axis. This was despite the fact that microspheres A and B never came in contact with each

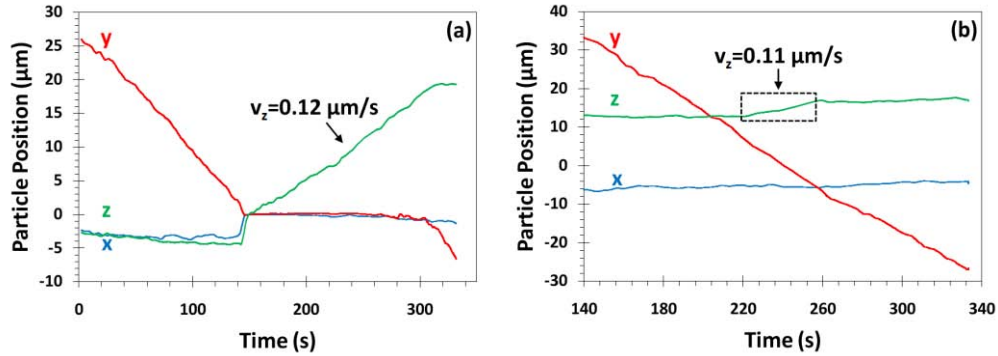


Fig. 3. Positions of (a) microsphere (A) and (b) microsphere (B), as a function of time. The origin of the coordinate system coincided with both the beam axis and the beam waist. Microsphere (A) became trapped in 2D, at $(x,y,z) = (0,0,z)$, and was then pushed in the positive z-direction. Microsphere (B) was not trapped, but was also pushed in the positive z-direction when within 8 μm of the beam axis.

other, as their radii were 1.6 μm and 1.7 μm , respectively (as measured using camera 1), but their closest center-to-center spacing was 7.5 μm . The difference in y-velocity between the two microspheres, despite their similar size, can be attributed to the creeping fluid flow in the negative y-direction, which would be expected to exhibit a parabolic velocity profile. This flow was estimated to have a peak y-velocity of 0.2 $\mu\text{m/s}$, by tracking the y-velocities of various microspheres of different size and location within the cell, and correcting for terminal velocity due to gravity.

3. Analysis

The resulting z-velocity of microsphere A is plotted versus position along the beam axis in Fig. 4(a). This curve was calculated by first fitting the position versus time data to a smoothed spline and then differentiating, which helped to reduce the effects of noise (though noise due to mechanical vibrations and particle tracking error was accentuated by differentiation, the overall trend is clear in both Figs. 3 and 4). As shown, microsphere A experienced a rapid acceleration towards the beam waist (at $z = 0$), which then all but vanished upon reaching the waist. Such behavior is qualitatively consistent with a 3D optical trap, which pushes a particle towards an equilibrium point located just beyond the beam waist via radiation pressure [17]. The motion observed beyond and away from the waist, in the region $z > 0$, was, however, inconsistent with a stable 3D trap.

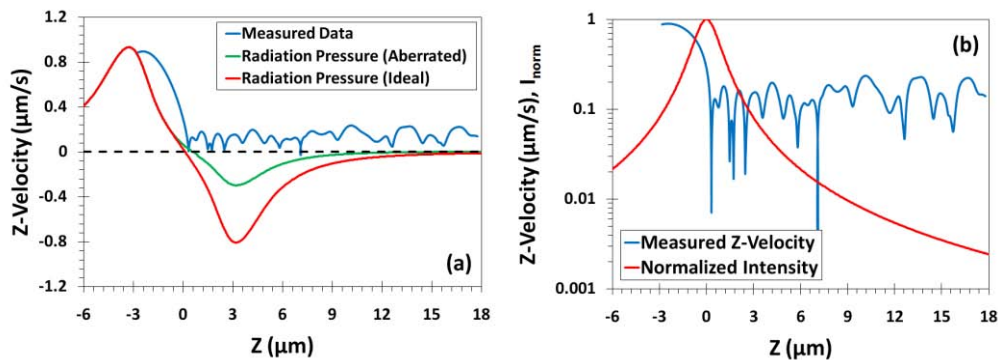


Fig. 4. Measured z-velocity versus axial position, compared to (a) the z-velocity predicted by radiation pressure, and (b) the local intensity of a Gaussian beam. In (a), the curve labeled “ideal” is based on rigorous calculations for an ideal beam, while the curve labeled “aberrated” is a qualitative estimate of the impact of weak spherical aberration.

3.1 Radiation pressure

In order to both illustrate that the observed motion was inconsistent with a stable 3D trap and to aid in further analysis, a series of theoretical calculations of the optical force due to radiation pressure were performed for microsphere **A**, using an approach based on Nieminen [24–26]. Since details of these calculations are not of immediate importance, the methodology has been summarized in Appendix A. Here it suffices to note that the calculations were performed assuming a 0.4 μm beam waist, 1.6 μm particle radius, 35 mW optical power, and liquid and particle refractive indices of 1.43 and 1.45, respectively. The calculated optical force \mathbf{F}_{RP} on the microsphere was subsequently converted to a velocity \mathbf{v}_{RP} using Stokes' drag relation

$$\vec{v}_{RP} = \frac{\vec{F}_{RP}}{6\pi\eta R}, \quad (4)$$

where η is the dynamic viscosity of the liquid, 0.055 kg/m·s [27], and R the radius of the sphere, 1.6 μm .

The velocity predicted for microsphere **A** as a function of position along the beam axis is plotted in Fig. 4(a). As shown, in the region $z \leq 0$ the measured velocity was in reasonably good agreement with that predicted due to radiation pressure, particularly in terms of its magnitude. On the opposite side of the waist, however, agreement was extremely poor. One could ask whether this discrepancy was due to an incorrect assumption of a perfect, aberration-free optical beam in the radiation pressure calculations. It is known that even slight spherical aberration along the optical path, which tends to blur the focused spot, will significantly weaken the axial restoring force on the positive z side of the waist [28,29]. In previous studies it has been shown that for weak spherical aberration, the forward force in the $z \leq 0$ region remains largely unchanged, while the reverse force for $z > 0$ is significantly reduced. Based on data presented in such works, we have included a *qualitative estimate* of how the velocity of the microspheres might have been impacted by slight spherical beam aberration. This serves to illustrate that the axial restoring force for $z > 0$ due to radiation pressure may have been significantly weaker than that predicted for the ideal beam. This is an important point, because the discrepancy between radiation pressure calculations and experiment in the region $z > 0$, both in magnitude and direction, force us to consider additional contributions to the motion of the particle, which must ultimately be reconciled with the restoring force due to radiation pressure. Spherical aberration was also to be expected in the experiment, since the lens was aberration-corrected for a 170 μm thick coverslip, but the experimental focus was only 39 μm into the sample cell. In the following subsection it will be shown that this qualitative estimate leads to a consistent description of the observed motion, in which radiation pressure dominates for $z < 0$ and thermophoresis dominates for $z > 8 \mu\text{m}$, despite reasonable uncertainty due to aberration in the region between.

Figure 4(b) compares the measured z -velocity of microsphere **A** to the normalized intensity along the beam axis, defined as $I_{norm} \equiv I(0,0,z)/I(0,0,0)$. As shown, the rapid $1/z^2$ roll-off in intensity for large z was very dissimilar to the relatively constant velocity observed from $z = 0$ to 18 μm . Based on this simple observation, a direct relationship between the local intensity and the observed motion in the range $z > 0$ could be ruled out. This was important, because it allowed a wide range of effects to be confidently ruled out, including indirect photophoresis, momentum transfer due to optical absorption within the particle, and radiation pressure, all of which would have produced forces proportional to either the local intensity or its gradient. Based on this result, it was necessary to consider an indirect relationship between the local intensity and the observed motion in the region $z > 0$.

3.2 Thermophoresis

A reasonable starting point was to consider the impact of optical absorption within the liquid. Optical absorption converts optical energy to heat within a material, according to the relation

$$Q = 2\alpha I \quad (5)$$

where Q is the change in heat density per unit time, 2α is the optical power absorption coefficient of the material, and I is the local intensity. This in turn is related to the local temperature T , through the heat equation [30]

$$\nabla \cdot (k \nabla T) + Q = 0, \quad (6)$$

and the boundary conditions

$$T_1 = T_2 \quad (7)$$

$$k_1 \hat{n} \cdot \nabla T_1 = k_2 \hat{n} \cdot \nabla T_2 \quad (8)$$

for an interface between materials 1 and 2. Here k represents the thermal conductivity of the material, and \hat{n} is the normal unit vector at the interface. Convective heat transfer has been neglected in Eq. (6), due to the extremely low fluid velocities observed in the experiment. Steady-state conditions have also been assumed.

In order to solve Eqs. (5) through (8), and obtain the temperature distribution within the sample cell, simulations were performed using commercially available 3D finite element software. Material and beam properties used in the simulations are provided in Table 1 (the power absorption coefficient for propylene glycol [22] was consistent with independent measurements performed using a spectrophotometer). The air-glass boundary was modeled using the heat flux boundary condition

$$k_c \hat{n} \cdot \nabla T = -h(T - T_\infty), \quad (9)$$

which approximated convective cooling of the cell by the surrounding air. The ends of the cell, located at $y = \pm 1.6$ mm in the simulation, were modeled as thermal insulators. For reasons to be given shortly, the temperature profile in the cell was modeled without taking the presence of any microspheres into account.

Table 1. Properties Used for Thermal Simulations

Symbol	Value	Description
λ_0	0.808 μm	Vacuum wavelength
ω_0	0.4 μm	Beam waist size
n_l	1.43	Refractive index of liquid [20]
P	35 mW	Optical power in liquid
$2\alpha_l$	2.9 m^{-1}	Power absorption coefficient of liquid [22]
$2\alpha_c$	0.1 m^{-1}	Power absorption coefficient of cell [20]
k_l	0.196 W/m·K	Thermal conductivity of liquid [27]
k_c	1.0 W/m·K	Thermal conductivity of cell [20]
h	40 W/m ² ·K	Heat transfer coefficient of air [31]
T_∞	293 K	Ambient temperature

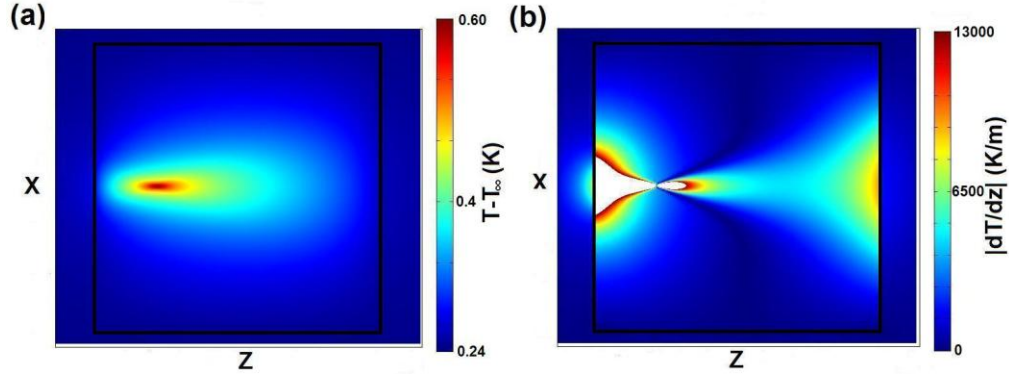


Fig. 5. Simulated (a) temperature T and (b) magnitude of the temperature gradient in the z -direction $|\partial T/\partial z|$, in the $y = 0$ plane. The black square marks the liquid-glass boundary, and had sides $50 \mu\text{m}$ long. The peak temperature was 0.60 K above ambient. The white regions of (b) represent regions where $|\partial T/\partial z|$ exceeds $13,000 \text{ K/m}$.

Figure 5(a) plots the resulting temperature distribution in the sample cell across the xz plane ($y = 0$). The magnitude of the z -component of the temperature gradient, $|\partial T/\partial z|$, is also plotted in Fig. 5(b). Note that the peak simulated temperature in the cell was only 0.60 K above the ambient temperature. This is significant because it indicates that temperature variations in the cell only weakly-perturbed the material properties in the experiment.

There are a number of theoretical models that relate the temperature gradient in a liquid to the particle velocity induced by thermophoresis [3–11]. The physics behind each can in principle be applied to an arbitrary temperature profile. However, calculations are greatly simplified if one can approximate a spatially uniform temperature gradient, ∇T_0 , where T_0 is the temperature in the *absence* of the particle. Under such a condition, each model yields an expression of the form

$$\vec{v}_T = -D_T \nabla T_0, \quad (10)$$

for the thermophoretic velocity of a spherical particle in a liquid. The thermal diffusivity D_T takes different forms for the different models, and will be discussed in greater detail in the following section. The present emphasis is on comparing the form of Eq. (10) to measured data.

In doing so, it is important to first note that the simulated temperature profile in Fig. 5(a) does not strictly adhere to the condition implicit in Eq. (10) of a spatially-uniform temperature gradient. However, for all models of thermophoresis to be considered, it is sufficient that ∇T_0 instead vary little over the extent of the particle to appropriately apply Eq. (10). This condition is reasonably well-satisfied for a $3.2 \mu\text{m}$ diameter particle near the center of the cell, and thus the latter portion of the trajectory of microsphere **A**. Closer to the beam waist, however, variations in the temperature gradient over the extent of this microsphere were expected to introduce error when applying Eq. (10). For microsphere **B** the rapid variation in the x and y components of the temperature gradient (nonexistent for microsphere **A**) would also have introduced error when using Eq. (10). Thus, in the following it is understood that the application of Eq. (10) to the temperature profile of Fig. 5(a) provides approximate results, except for the latter portion of the trajectory of microsphere **A** where error should be negligible. Furthermore, the presence of each microsphere in the liquid would have altered the temperature profile, not only due to heat conduction, which is accounted for in D_T , but also by altering the local heat density \mathcal{Q} , due to the negligible optical absorption of the particle. This effect was most pronounced when the sphere is at the beam focus, but elsewhere relatively weak.

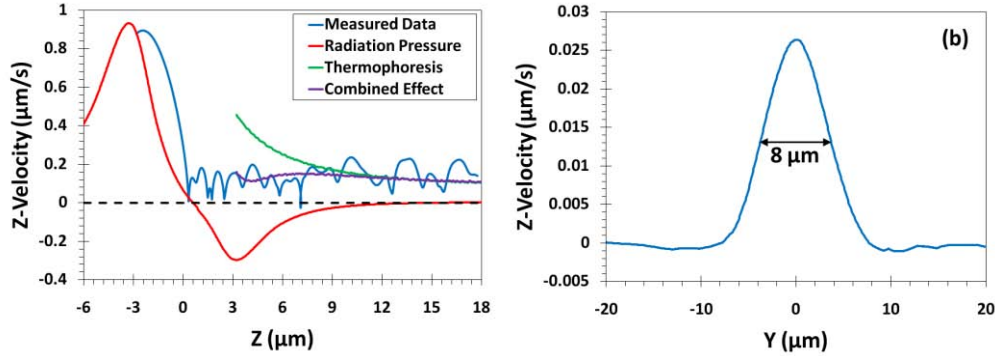


Fig. 6. (a) Comparison of the measured z-velocity of microsphere (A) along the beam axis with predicted velocities due to thermophoresis, radiation pressure, and the combined effect of thermophoresis and radiation pressure, and (b) the predicted thermophoretic z-velocity of microsphere (B) versus y position. The radiation pressure curve in (a) matches the estimated plot for an aberrated beam in Fig. 4(a).

The thermophoretic velocity of microsphere **A** at different points along the beam axis was calculated using Eq. (10) and the simulated temperature gradient, and is plotted in Fig. 6(a). For this calculation a thermal diffusivity of $D_T = 22 \mu\text{m}^2/\text{s}\cdot\text{K}$ was assumed in order to provide a best fit to the measured data, which will later be shown to be consistent with theory. Note that velocity predictions have been omitted very close to the beam waist, where ∇T_0 varied substantially over the extent of a $3.2 \mu\text{m}$ diameter microsphere, and where the (relatively low) absorption of the microsphere would have most impacted the thermal profile. Figure 6(a) also plots the measured velocity of microsphere **A**, and the estimated velocity due to radiation pressure from Fig. 4(a) for an aberrated beam. The most important result of Fig. 6(a) is that thermophoresis accounts for the observed nonzero velocity of the particle far from the beam waist, where radiation pressure falls out of consideration. Also significant is that the combined effect of radiation pressure and thermophoresis, plotted as the sum of the two velocities in the figure, adequately describes the relatively constant velocity observed in the experiment, over a range where the local intensity varied by over an order of magnitude. Although the radiation pressure in Fig. 6(a) was merely an estimate (for $z > 0$), the resulting agreement between theory and experiment provides justification for its use.

Figure 6(a) presents compelling evidence that the particle motion observed in the region $z > 3 \mu\text{m}$ was dominated by thermophoresis, but it does not constitute conclusive proof. The case can be strengthened, however, by considering the trajectory of microsphere **B**. This sphere fell continuously along a path that remained constant in x ($x = -5.5 \mu\text{m}$), but varied slightly in z ($z = 13$ to $17 \mu\text{m}$), due to a positive z-velocity that was only discernible over the limited range $y = -6$ to $6 \mu\text{m}$. For the purpose of comparison, Fig. 6(b) plots the thermophoretic z-velocity predicted for a similar path, along the line $(x, z) = (-5.5, 15) \mu\text{m}$. This figure shows that thermophoresis should only have been significant over a very similar range of y . The slight discrepancy between the predicted $8 \mu\text{m}$ FWHM interaction region and the measured $12 \mu\text{m}$ range was easily attributable to the variation in ∇T over the $3.4 \mu\text{m}$ diameter of the sphere. Such agreement between the measured particle velocity and the local temperature gradient, along multiple axes, provides strong support for the conclusion that the observed motion in the region $z > 3 \mu\text{m}$ was due to thermophoresis.

3.3 Transfer of optical momentum to the liquid

For completeness, it is also worth noting that optical momentum absorbed by the liquid can induce convective flow, an effect known to be significant under certain (but different) circumstances [32]. Given that the linear momentum flux of the optical beam is given by Sn/c , where S is the Poynting vector and c the vacuum speed of light, it can easily be shown that absorption of optical momentum by the liquid produces to the local force density

$$\vec{f}_{abs} \cong (2\alpha I n_l / c) \hat{z}. \quad (11)$$

The convection currents generated by this force density within the sample cell were estimated by performing 3D fluid dynamics simulations, based on the Navier-Stokes equations, using commercial finite element modeling software. Figure (7) plots the resulting z-velocity profile of the liquid in the $y = 0$ plane. As shown, the peak velocity was $0.0036 \mu\text{m/s}$, which was less than 3% that measured in the experiment. A similar result follows from an approximate model based on Poiseuille flow, described in Appendix B. The observed particle motion was therefore not attributable to absorption of optical momentum by the liquid, but was instead consistent with thermophoresis. Independent simulations of natural (buoyant) convection were also performed to show that its effect was negligible.

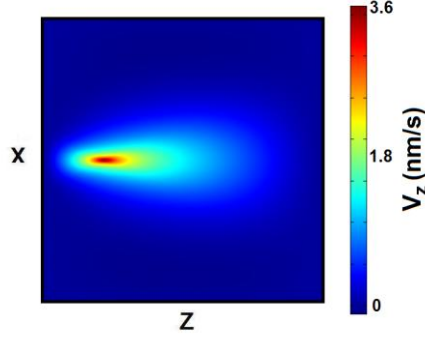


Fig. 7. Simulated z-velocity of the liquid in sample cell, resulting from the transfer of optical momentum to the liquid due to optical absorption. Velocities shown are for the $y = 0$ plane. The black square marks the liquid-glass boundary, which had sides $50 \mu\text{m}$ long.

4. Discussion

At this point a comparison between the thermal diffusivity D_T used in the preceding calculation with that of various theoretical models is in order. For this purpose, we consider models proposed by McNab and Meisen [4], Schimpf and Semenov [3,6], Ruckenstein [8,9], Duhr and Braun [10], and Brenner [3], for which the thermal diffusivities, denoted D_{TM} , D_{TS} , D_{TR} , D_{TD} and D_{TB} , respectively, are given by

$$D_{TM} = \frac{0.13\eta}{\rho T \left[1 + (k_p / 2k_l) \right]} \quad (12)$$

$$D_{TS} = \frac{(\ln 3) \sqrt{A_p A_t}}{64\eta r_l \left[1 + (k_p / 2k_l) \right]} \quad (13)$$

$$D_{TR} = \frac{2\xi}{3\eta} \frac{\partial \gamma}{\partial T} \quad (14)$$

$$D_{TD} = \frac{R\sigma_{eff}^2 \lambda_{DH}}{6\eta \epsilon_R \epsilon_0 T} \left(1 - \frac{T}{\epsilon_R} \frac{\partial \epsilon_R}{\partial T} \right) \quad (15)$$

Table 2. Material Properties Used for Model Comparison

Symbol	Value	Description
ρ	1033 kg/m ³	Density of liquid [20]
T_∞	293 K	Ambient temperature
k_p	1.35 W/m·K	Thermal conductivity of particle [20]
β	7.0x10 ⁻⁴ K ⁻¹	Volumetric thermal expansion coefficient of liquid [20]
c_p	2470 J/kg·K	Isobaric specific heat of liquid [20]
r_l	0.25 nm	Molecular radius of liquid
A_p	6.5x10 ⁻²⁰ J	Hamaker constant of particle [33]
A_l	5.6x10 ⁻²⁰ J	Hamaker constant of liquid [34]
ϵ_R	29.3	Relative permittivity of liquid [20]
$\partial\epsilon_R/\partial T$	-0.181 K ⁻¹	[20]
λ_{DH}	1.1 μm	Debye length of liquid (derived from [36,37])
D_{TM}	5300 $\mu\text{m}^2/\text{s}\cdot\text{K}$	Thermal diffusivity from McNab-Meisen model
D_{TS}	0.012 $\mu\text{m}^2/\text{s}\cdot\text{K}$	Thermal diffusivity from Schimpf-Semenov model
D_{TB}	13 $\mu\text{m}^2/\text{s}\cdot\text{K}$	Thermal diffusivity from Brenner model

$$D_{TB} = \frac{k_l \beta}{\rho c_p \left[1 + (k_p / 2k_l) \right]} \quad (16)$$

In these expressions, ρ , β , c_p , ϵ_R , r_l and λ_{DH} represent the liquid's density, volumetric thermal expansion coefficient, isobaric specific heat, relative permittivity, molecular radius, and Debye length, respectively, and k_p is the particle's thermal conductivity. The Hamaker constants for the particle and liquid are denoted as A_p and A_l . Table 2 lists the relevant quantities for propylene glycol and silica, as well as the computed thermal diffusivities. As the interfacial tension of the propylene glycol-silica interface γ , and the interaction layer thickness ζ were not known [1], D_{TR} was excluded from Table 2, but is discussed below. As the effective surface charge per unit area of the microsphere σ_{eff} was also unknown, D_{TD} is also discussed independently below.

4.1 The McNab-Meisen model

The McNab-Meisen model, which is simply a scaled version of a model for thermophoresis in gases, has been included here because it was shown to accurately model the thermophoretic velocity of individual 0.8-1.0 μm diameter polystyrene microspheres in water [4]. As shown in Table 2, the predicted value for D_{TM} exceeds the experimentally-fit value of 22 $\mu\text{m}^2/\text{s}\cdot\text{K}$ by over two orders of magnitude, so this model could not be regarded as consistent with the measured data.

4.2 The Schimpf-Semenov dipole-dipole model

The Schimpf-Semenov model is based on dipole-dipole interactions between the liquid and particle, and was originally developed for particles of similar size to the liquid molecules themselves [3]. However, it was extended to larger particles by Brenner [3] in his derivation of the modified form of Eq. (13). In Table 2 it is shown that the predicted value D_{TS} was over two orders of magnitude lower than the experimentally-fit value of 22 $\mu\text{m}^2/\text{s}\cdot\text{K}$. Thus, the Schimpf-Semenov model was inconsistent with the thermophoretic motion observed in the experiment.

4.3 The Ruckenstein model

The Ruckenstein model is based on the presumption that temperature-induced variations in the interfacial tension at a liquid-solid interface drive thermophoresis [8,9]. Although data for the interfacial tension at a propylene glycol-silica interface was not known to be available in the literature, the fact that the contact angle between propylene glycol and silica is small allowed the interfacial tension to be approximated as the negative of propylene glycol's surface tension. Using data from [35], this led to the result $\partial\gamma/\partial T \approx 7 \times 10^{-5}$ N/m·K for propylene glycol. In order to match D_{TR} to the experimentally-fit value 22 $\mu\text{m}^2/\text{s}\cdot\text{K}$, the

interaction layer thickness ξ then needed to be 26 nm. By way of comparison, if the same procedure were performed for water and silica, using the measured thermal diffusivity $22 \mu\text{m}^2/\text{s}\cdot\text{K}$ for silica in pure, deionized water [14], and the interfacial tension $\partial\gamma/\partial T \approx 1.6 \times 10^{-4} \text{ N/m}\cdot\text{K}$ [20], the interaction layer thickness would instead have been 0.18 nm. Given the implausibility that the interaction layer thickness for interfacial tension should vary so substantially between the two similar liquids, the Ruckenstein model was not regarded as a viable explanation for the observed thermophoretic motion.

4.4 The Duhr-Braun ionic-shielding model

The Duhr-Braun model ionic-shielding model is based on the concept that under conditions of local thermodynamic equilibrium and constant pressure, steady-state thermo-diffusion will be directly related to the entropy of the particle-solvent system [10,15]. For liquids with sufficiently weak ionic concentration (such as pure propylene glycol), this leads to a thermal diffusivity that is proportional to the Debye length. However, in order to satisfy conditions of local thermodynamic equilibrium, it is necessary that the temperature gradient be limited to the range [10]

$$|\nabla T| < \frac{k_B T}{6\pi\eta R^2 D_T}, \quad (17)$$

or equivalently, through Eq. (10), that the thermophoretic velocity be limited to

$$|\vec{v}_T| < \frac{k_B T}{6\pi\eta R^2}, \quad (18)$$

where k_B is Boltzmann's constant. For conditions in the experiment, these limits were $|\nabla T| < 69 \text{ K/m}$ and $|\vec{v}_T| < 0.0015 \mu\text{m/s}$, respectively, or nearly two orders of magnitude below those measured/simulated. Thus, a treatment of thermophoresis based on a local thermodynamic equilibrium was not appropriate given the conditions of the experiment.

4.5 The Brenner model

The Brenner model, in its most basic form [11], is based on a proposed (yet experimentally unconfirmed) thermal creep boundary condition at the liquid-particle interface, which directly leads to particle thermophoresis. The expression in Eq. (16) also embodies a novel interpretation of the nature of viscous stress in non-isothermal fluids [3]. Table 2 shows that the predicted value D_{TB} was within a factor of 1.8 of the experimentally-fit value $22 \mu\text{m}^2/\text{s}\cdot\text{K}$. This small discrepancy could be attributed to the non-uniformity of ∇T_0 in the experiment, or inaccuracy of the absorption coefficient $2\alpha_l$ and/or heat transfer coefficient h used in the thermal model. It also may be due to the fact that Eq. (16) did not account for "generation of volume" in the experiment due to optical absorption (for a discussion of this effect see [38]). Nonetheless, the relatively good agreement demonstrates a sound theoretical basis for the thermophoretic calculations presented in Section 3. Additionally, these results provide support for the Brenner model of thermophoresis, which has not been rigorously tested due to the scarcity of experimental data for thermophoretic motion of individual particles in a liquid [3,5].

5. Extension to small particles in an optical trap

In the context of optical trapping and manipulation of small particles in liquids, these results are significant in that they demonstrate that laser-induced thermophoresis can under certain circumstances dominate the effects of radiation pressure in a conventional optical trap. Furthermore, they support a theoretical model that can be used to quantify the impact of thermophoresis for individual particles. In order to expand upon these points, we consider an *effective* thermophoretic force acting on a spherical particle in a temperature gradient, defined in analogy to Eq. (4), as

$$\vec{F}_{Teq} = 6\pi\eta R\vec{v}_T. \quad (19)$$

This quantity is referred to as an “effective” force because it does not necessarily represent the physics behind thermophoresis. It does, however, accurately describe the thermophoretic contribution to the net force on a particle, under the common assumption that the net force is related to the particle velocity according to Stokes’ law. By combining Eqs. (10) and (19), the effective thermophoretic force can be related directly to the temperature gradient,

$$\vec{F}_{Teq} = -6\pi\eta R D_T \nabla T_0. \quad (20)$$

This quantity is predicted from Eq. (16) to scale linearly with the particle radius R . Such scaling is also supported by a body of work on thermo-diffusion, which indicates that D_T is for the most part independent of R in the quasi-hydrodynamic limit [1] (with the notable exception of strongly-electrolytic solutions [10]). In contrast, radiation pressure produces a force which in the small particle limit is given by [17]

$$\vec{F}_{RP} = \frac{2\pi R^3}{c} \left(\frac{n_p^2 - n_l^2}{n_p^2 + 2n_l^2} \right) \nabla I + \frac{128\pi^5 n_l R^6}{3\lambda_0^4 c} \left(\frac{n_p^2 - n_l^2}{n_p^2 + 2n_l^2} \right)^2 I, \quad (21)$$

and which scales at least as R^3 . Thus, with decreasing particle size, thermophoresis can eventually dominate.

In the simulations presented in Section 3, the intensity gradient in the z-direction had peak value $0.105 \text{ W}/\mu\text{m}^3$. At the same position the temperature gradient was $0.041 \text{ K}/\mu\text{m}$. Using these values as an example, along with material properties already provided, the magnitudes of both the effective thermophoretic force and the maximum force due to radiation pressure were calculated for propylene glycol and silica, from Eqs. (20) and (21), and $D_T = 22 \text{ }\mu\text{m}^2/\text{s}\cdot\text{K}$, and plotted versus particle radius in Fig. 8(a). This figure also plots the force due to radiation pressure for a polystyrene particle with refractive index 1.58. Also included are the effective thermophoretic forces for power absorption coefficient of 19 m^{-1} , which closely matches that of both propylene glycol and water at 1064 nm, and the power absorption coefficient 4900 m^{-1} , matching that of water at 1480 nm. Note that the latter two curves provide a comparison of the *relative* impact of thermophoresis and radiation pressure. However, in practice, temperature constraints may limit the optical power that can be used, in which case both forces would decrease linearly with P .

Figure 8(a) predicts that for silica particles suspended in propylene glycol (under stated conditions), thermophoresis will dominate the axial radiation pressure throughout the nano-scale ($R \leq 100 \text{ nm}$). For a Gaussian beam, the effective thermophoretic force is directed away from the focus, such that thermophoresis serves to inhibit trapping in 3D. Thus, the ability (or inability) of a Gaussian beam to trap small particles depends not only on random thermal motion, governed by $k_B T$, but also on the effective thermophoretic force.

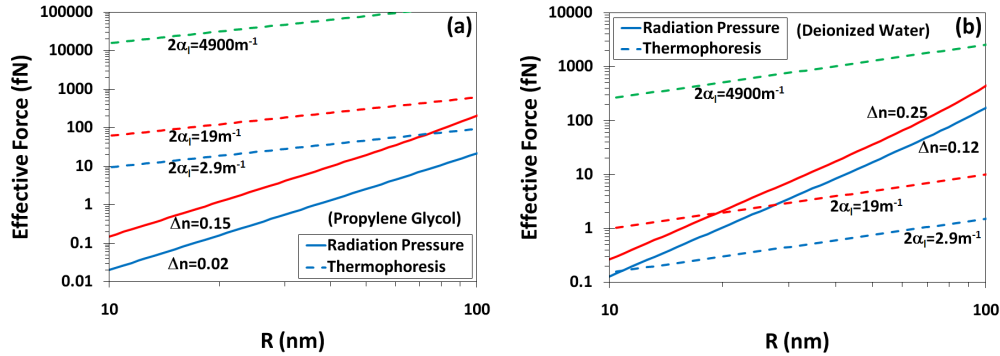


Fig. 8. Predicted values of the peak radiation pressure force and the effective thermophoretic force, along the beam axis, for an individual silica nano-sphere in pure (a) propylene glycol and (b) deionized water. For the range of particle radii shown, the thermophoretic force dominates in propylene glycol. For deionized water the thermophoretic force is substantially reduced, but still dominates for smaller particle radii.

For the purpose of comparison, Fig. 8(b) plots similar curves for a silica nano-sphere immersed in pure, deionized water, calculated using published values for the thermal diffusivity, $22 \mu\text{m}^2/\text{s}\cdot\text{K}$ [14], refractive index, 1.33 [20], and dynamic viscosity, $0.00089 \text{ kg/m}\cdot\text{s}$ [20]. For simplicity, the intensity and temperature gradients used in these calculations were identical to those used for propylene glycol ($0.105 \text{ W}/\mu\text{m}^3$ and $0.041 \text{ K}/\mu\text{m}$, respectively), although both would have been slightly different in water. As shown in Fig. 8, the effective thermophoretic force is predicted to be much weaker in deionized water than in propylene glycol. This is a consequence of the fact that the thermal diffusivities of the two liquids, both $22 \mu\text{m}^2/\text{s}\cdot\text{K}$, are remarkably similar. According to Eq. (20), for an identical particle radius and temperature gradient, the effective thermophoretic force should thus be roughly sixty times larger in propylene glycol than in deionized water (due to the relatively low viscosity of water). That is, the thermophoretic force scales with viscosity, since the thermal diffusivity, apparently, does not. Such a concept may seem counterintuitive, but would appear to be consistent with Brenner's theories on the nature of viscous stress in a non-isothermal fluid, and thermophoresis in general [3,11,38].

In its practical application, it should be noted from Fig. 8(b) that the thermophoretic force on a silica sphere in pure, deionized water can, but will not necessarily, dominate the force due to radiation pressure. For higher viscosity liquids, on the other hand, the relative strength of the effective thermophoretic force offers potential advantages for the control of individual particles on the nano-scale.

6. Conclusion

This paper has presented a detailed investigation of the motion of individual micro-particles in a moderately-viscous liquid in direct response to a local, laser-induced temperature gradient. The elevated viscosity of the liquid provided for substantial differences in the behavior predicted by various models of thermophoresis, which in turn allowed measured data to be most appropriately matched to a model proposed by Brenner. Based on this model, we have quantitatively predicted when thermophoresis will strongly inhibit the ability of radiation pressure to trap nano-scale particles. Furthermore, the model predicts that the thermophoretic force will scale linearly with the liquid viscosity, such that choice of liquid plays a key role in the relative strength of the thermophoretic and radiation forces.

Appendix A

We calculate the axial trapping force on the particle using the method outlined by Nieminen *et al* in [24]. Briefly, the incident beam is written as a sum of vector spherical wavefunctions (VSWFs) where the coefficients of the VSWFs that correspond to the incident Gaussian beam

are calculated using a point-matching procedure in the far field [25]. First, the far field limit for a paraxial y-polarized Gaussian beam as a function of the beam waist is used to estimate the field at a defined set of points. The VSWFs are then calculated at each of those points and the resulting overdetermined system of equations is solved in a least-squares sense for the coefficients of the VSWF basis.

Once the VSWF coefficients are determined, forces on the particle are calculated using a T-matrix approach [26], where the expansion coefficients of the scattered wave, \mathbf{P} , are written as a function of the incident beam coefficients, \mathbf{A} , and the T-matrix as $\mathbf{P}=\mathbf{TA}$. For a spherical particle, the T-matrix is diagonal with elements given by the usual Mie coefficients. Given the incident and scattered coefficients, the force and torque on the particle can be computed [24].

We note that the incident coefficients corresponding to a single origin and orientation need only be calculated once using the point-matching procedure. Once these have been determined, the coefficients corresponding to other spatial locations in the same trapping field can be determined using coordinate transformations and rotations of the VSWFs [24]. We first determine the coefficients for a VSWF basis centered at the beam waist and then predict the forces corresponding to particle locations at various points along the axis of the beam.

Appendix B

From Eq. (11), the optical momentum absorbed by the liquid produces a force per unit length across the cross-section of the optical beam of

$$\frac{\partial \vec{F}_{abs}}{\partial z} = \int_{-\infty}^{\infty} \int_{-\infty}^{\infty} \vec{f}_{abs} dx dy = \frac{2\alpha P n_l \hat{z}}{c}. \quad (\text{B1})$$

In comparison, the laminar flow of liquid through a circular channel of radius $a_{channel}$, assuming no-slip boundary conditions, is related to the force per unit length across the channel [39]

$$\frac{\partial \vec{F}_{flow}}{\partial z} = \frac{\partial p}{\partial z} (\pi a_{channel}^2) \hat{z} = 4\pi\eta \vec{v}_{max}, \quad (\text{B2})$$

where p is the fluid pressure and \vec{v}_{max} the peak velocity of the liquid. Equating Eqs. (B1) and (B2) leads to a rough estimate of the fluid flow resulting from the absorption of optical momentum by the liquid

$$\vec{v}_{max} \sim \frac{\alpha P n_l \hat{z}}{2\pi\eta c}. \quad (\text{B3})$$

When related to experimental conditions, this predicts a peak velocity of 0.0007 $\mu\text{m/s}$, which was within a factor of 5 of that determined by the more rigorous finite element simulations.